



# Bismuth and cerium doped cryptomelane-type manganese dioxide nanorods as bifunctional catalysts for rechargeable alkaline metal-air batteries

N. Vilas Bôas, J. Batista Souza Junior, L. Carlos Varanda, S. Antonio Spinola Machado, M. Luiz Calegari\*

Instituto de Química de São Carlos, Universidade de São Paulo, São Carlos 13566-590, Caixa Postal 780, SP, Brazil

## ARTICLE INFO

### Keywords:

Oxygen reduction reaction  
Oxygen evolution reaction  
Cation doped manganese dioxide  
Zinc/air batteries  
Alkaline fuel cells

## ABSTRACT

Metal-air batteries are energy storage devices (ESD) used in many technological applications ranging from portable, wearable to stationary, owing to its simplicity and low cost. Manganese oxides are suitable materials to be used as electrodes in such devices presenting an electrocatalytic performance for oxygen reactions close to Pt and, most importantly, being a low cost, abundant and environmentally friendly material. However, as a drawback, manganese dioxide has low electrical conductivity thus requiring the combination with some highly conductive carbon support to be efficiently used as catalyst for the oxygen reactions in ESD. The low stability of carbon for water splitting reaction, however, limits the  $\text{MnO}_2$  to act as bifunctional catalyst. In this work, to overcome this problem, three and tetravalent cation doped ( $\text{Bi}^{3+}$ ,  $\text{Ce}^{4+}$ ) manganese dioxide nanorods exhibiting higher electrical conductivity were prepared and used as carbon free electrocatalysts for the oxygen reduction and evolution reactions in alkaline medium. X-ray power diffraction (XRD), Transmission Electron Microscopy (TEM), X-ray Photoelectron Spectroscopy (XPS) and Diffuse Reflectance Spectroscopy (DRS) measurements were performed to determine the structure, morphology, surface chemical composition and band gap values of the catalysts confirming the formation of nanorod structures with lower band gap values ( $E_{\text{BG}}$ ). The electrochemical results of  $\text{Bi}^{3+}$  and  $\text{Ce}^{4+}$  doped  $\text{MnO}_2$  confirmed that these materials have higher conductivity than  $\text{K}^{+1}$  doped  $\text{MnO}_2$  in agreement with the lower  $E_{\text{BG}}$  inferred from DRS measurements. The electrocatalytic performance of doped electrocatalysts for the OER was close to that reported for conventional  $\text{MnO}_2/\text{C}$  catalysts. On the other hand, they presented a remarkable performance for the ORR, higher than that presented by a commercial state of art Pt/C catalyst. The excellent catalytic performance was confirmed by Zn-air mini battery tests which presented a peak power density of  $45 \text{ mW cm}^{-2}$ , higher than that presented by a conventional  $\text{MnO}_2/\text{C}$  50 wt.% catalyst ( $40 \text{ mW cm}^{-2}$ ).

## 1. Introduction

The human society has experienced as never the benefits provided by remarkable technological advances achieved in the last years. From entertainment to health monitoring, a variety of portable devices are now accessible to users. However, one of the most relevant challenges is the inherent requirement of an efficient and non-expensive source of electric power. In fact, the demand for energy is one of the most critical aspects and has mobilized the scientific community to find new options of sustainable energy conversion and storage devices. Accordingly, metal-air batteries are among the most interesting and promising alternative power sources [1–6]. The further development of such devices is dependent on the improvement of some critical components, being the catalysts development the action that demands more attention. The

efficiency of energy conversion depends directly on the efficiency of the catalysts operating as electrodes in such devices.

Cathode catalyst requires the main attention in metal-air batteries as its performance is limited by the ability of the catalyst to efficiently reduce oxygen to hydroxyl ions [7]. Carbon powder and carbon dispersed manganese dioxide have been tested as cathode catalysts in metal-air batteries. In fact, manganese dioxide is a strategic material in energy conversion devices, presenting very low cost and abundance in natural ores, high environmental compatibility, low toxicity and especially a high electrocatalytic activity for both the oxygen reduction reaction (ORR) and oxygen evolution reaction (OER) [8]. All these advantages justify the increasing attention presented by the scientific community expressed by the number of recent publications related to  $\text{MnO}_2$  as a bifunctional air catalyst [9–14]. However, pure  $\text{MnO}_2$  and

\* Corresponding author.

E-mail address: [calegari@iqsc.usp.br](mailto:calegari@iqsc.usp.br) (M.L. Calegari).

<https://doi.org/10.1016/j.apcatb.2019.118014>

Received 11 September 2018; Received in revised form 28 January 2019; Accepted 27 July 2019

Available online 29 July 2019

0926-3373/© 2019 Elsevier B.V. All rights reserved.

mostly of the transition metal oxides materials present low electrical conductivity. One way to overcome this problem is using  $\text{MnO}_2$  composites with some appropriate electrical conductor like a high surface area carbon powder [15]. The problem is that carbon powder is unstable in the potential range required for the OER. In such high potential values, carbon is gradually oxidized to  $\text{CO}_2$ , lowering the cathode catalyst efficiency and the battery performance. A possible strategy to overcome such limitation is by improving the oxide conductivity. One elegant possibility is doping  $\text{MnO}_2$  with appropriate metallic cations. The resulting doped materials could be adequate to operate efficiently as a bifunctional cathode catalyst in rechargeable metal-air batteries and alkaline fuel cells without the need to include carbon in the formulation.

In this way,  $\alpha\text{-MnO}_2$ , known as cryptomelane or octahedral molecular sieves (OMS-2), has a unique crystallographic structure that presents a  $(2 \times 2)$  tunnel framework along the  $c$ -axis related to the  $[001]$  direction and centered on the  $ab$ -plane of the unit cell. The tunnel structure is a channel for ions and molecules and can be used to dope the  $\alpha\text{-MnO}_2$  structure changing its electrical properties. In fact, the  $\alpha\text{-MnO}_2$  structure is supported by the presence of water and cations inside the  $(2 \times 2)$  tunnel, otherwise the structure can collapse to the  $\beta\text{-MnO}_2$  [16]. Several reports can be found in the literature relating the doping the OMS-2 with monovalent cations like  $\text{Na}^+$ ,  $\text{Li}^+$ , and  $\text{K}^+$ . However, few studies have been found employing trivalent ( $\text{M}^{3+}$ ) and tetravalent ( $\text{M}^{4+}$ ) metal cations. In this study,  $\text{Bi}^{3+}$  and  $\text{Ce}^{4+}$  doped  $\alpha\text{-MnO}_2$  nanorods are used as unsupported catalyst for the ORR and OER. The materials are physically characterized by transmission electron microscopy, X ray powder diffraction and diffuse reflectance spectroscopy. The electrochemical characterization is initially performed by cyclic voltammetry and by quasi steady-state polarization curves using the rotating disk electrode system and the materials are further evaluated as cathode catalysts in a mini Zn-air battery by polarization curves and electrochemical impedance spectroscopy techniques.

## 2. Experimental

### 2.1. Materials

Potassium permanganate (99.0%) was purchased from Merck, potassium hydroxide (88.0%) from J. T. Baker, Printex 6L carbon was purchased from Degussa, nitric acid (65%) from Synth, Nafion® (5%), bismuth nitrate pentahydrate (98%), cerium IV ammoniacal nitrate (99.9%) were acquired from Sigma-Aldrich. All reagents used in this work were of analytical grade and used without any further purification. All solutions were prepared with pure water with a resistivity higher than  $18.2 \text{ M}\Omega \text{ cm}^{-1}$  obtained from a Barnstead Nanopure system.

### 2.2. Synthesis of $\text{MnO}_2$ nanorods

Manganese dioxide nanorods were prepared following the method proposed by Deguzman et al. [17]. Briefly, a solution is prepared by dissolving  $\text{KMnO}_4$  (5.89 g, 42.7 mmol) in  $\text{H}_2\text{O}$  (10 mL) and mixed in a round bottom flask with another solution composed  $\text{MnSO}_4 \cdot \text{H}_2\text{O}$  (8.8 g, 52.1 mmol) dissolved in concentrate  $\text{HNO}_3$  (30 mL). The resulting mixture is then submitted to reflux at  $95^\circ\text{C}$  for 24 h. The final product, a dark brown powder, is filtered, exhaustively washed with water and dried in an oven at  $120^\circ\text{C}$ . The product prepared by this methodology is designated as OMS-2.

### 2.3. Synthesis of Bi or Ce doped $\text{MnO}_2$ nanorods

The Bi or Ce doped catalysts were prepared following also the method proposed by Deguzman et al. [17] with few modifications. For Bi doping,  $\text{KMnO}_4$  and  $\text{MnSO}_4 \cdot \text{H}_2\text{O}$  aqueous solutions are prepared as described before and mixed with a  $\text{Bi}(\text{NO}_3)_3 \cdot 5\text{H}_2\text{O}$  aqueous solution.

The resulting solution is then submitted to reflux at  $95^\circ\text{C}$  for 24 h. For Ce doping, an acidic  $\text{H}_2\text{SO}_4$  solution ( $1.0 \text{ mol L}^{-1}$ ) of  $(\text{NH}_4)_2\text{Ce}(\text{NO}_3)_6$  is firstly prepared and then a certain amount of OSM-2 nanorods previously prepared is added to the  $\text{Ce}^{4+}$  solution. The doping process occur by cation exchange process where,  $\text{K}^+$  cations are partially replaced by  $\text{Ce}^{4+}$  cations in the original structure generating the doped oxide. In both cases, the doping precursor,  $\text{Bi}(\text{NO}_3)_3 \cdot 5\text{H}_2\text{O}$  or  $(\text{NH}_4)_2\text{Ce}(\text{NO}_3)_6$  is added in an amount enough to produce a final concentration of  $0.01 \text{ mol L}^{-1}$   $\text{Bi}^{3+}$  or  $\text{Ce}^{4+}$ . The final products, a dark brown powder typical of OMS-2 materials, are filtered, exhaustively washed with water and dried in an oven at  $120^\circ\text{C}$ . The final product is designated as BiOMS-2 or CeOMS-2, depending on the cation used as dopant.

### 2.4. Materials characterizations

The morphology of the catalysts was evaluated by SEM using a LEO model 440 microscope and by TEM using a JEOL model JEM-2100 microscope operating at 200 kV generated by a  $\text{LaB}_6$  filament. For the TEM analysis, the samples were previously deposited onto the surface of a copper grid covered by a carbon film and Formvar.

Structural characterization was conducted by X ray powder diffraction using a Bruker D8 Advance equipment operating at 40 kV and 40 mA using the  $\text{CuK}\alpha$  ( $\lambda = 1.5425 \text{ \AA}$ ) radiation. The crystal structures were refined by the Rietveld method [18] using the DIFFRAC TOPAS v5 software solution from Bruker. The Launch mode was used to obtain the Fourier maps using an input file (INP) generated after the Rietveld refinement, where the doped OMS-2 structure was used to determine  $|F_{\text{obs}}|$  and a model  $\alpha\text{-MnO}_2$  structure, without the cation and the water in the site positions, was used to determine  $|F_{\text{calc}}|$  Fourier maps.

The chemical surface analysis for the oxides samples was performed by X-ray photoelectron spectroscopy (XPS) using a conventional XPS spectrometer (ScientaOmicron ESCA+) with a high-performance hemispheric analyzer (EAC2000) with monochromatic  $\text{Al K}\alpha$  ( $h\nu = 1486.6 \text{ eV}$ ) radiation as the excitation source. The operating pressure in the ultra-high vacuum chamber (UHV) during the analysis was  $1 \times 10^{-9} \text{ Pa}$ . The XPS high resolution spectra were recorded at constant pass energy of 20 eV with a 0.05 eV per step.

UV-Vis spectroscopy was conducted by a LAMBDA 35 Series UV/Vis Spectrophotometer from Perkin Elmer using a diluted sample dispersion keeping the maximum absorption below 0.1 to minimize the scattering signal. The Diffuse Reflectance Spectroscopy (DRS) measurements were carried out with a UV-vis Varian Cary 5G spectrometer using a quartz window and a polytetrafluorethylene pattern as reference. The obtained data were treated using the F(R) Schuster-Kubelka-Munk function.

### 2.5. Electrochemical characterization

The electrochemical characterizations were performed using a conventional three electrode cell. First, catalyst suspensions were prepared by mixing the catalyst powder (25 mg) in water (10 mL) containing a Nafion® perfluorinated resin solution (20  $\mu\text{L}$ , 5 wt.% in lower aliphatic alcohols and water). The working electrode was constructed by drop casting a volume of these suspensions (25  $\mu\text{L}$ ) on the top of a glassy carbon rotating disk electrode. The auxiliary electrode was a Pt foil ( $2.0 \text{ cm}^2$  geometric area) while the reference system was a  $\text{Hg}/\text{HgO}$  electrode.

The catalysts were analyzed by cyclic voltammetry using an aqueous  $\text{KOH}$  solution ( $1.0 \text{ mol L}^{-1}$ ) conducted at  $10 \text{ mV s}^{-1}$  in a potential range enough to fully characterize the different materials and avoiding the catalyst deactivation [19]. Polarization curves obtained at  $3 \text{ mV s}^{-1}$  were used to study the kinetics of ORR and OER. For the ORR, a rotating disk electrode (RDE) was used and the polarization curves were recorded at different electrode rotation rates (100, 200, 400, 625, 900, 1600 and 2500 rpm), while for the OER the electrode was kept static, without rotation.

The electrochemical measurements were conducted at room temperature using a PGSTAT128 Autolab electrochemical system (Eco Chemie, Utrecht, The Netherlands) programed by the NOVA v1.10 software (Eco Chemie, Utrecht, The Netherlands). The hydrodynamic experiments were performed using a commercial glassy carbon rotating disk electrode (Pine Instruments Co. System) with a geometric area of 0.2475 cm<sup>2</sup>. The electrode rotation speeds were controlled by an AFMSRE/ASR (Pine Instruments Co. System) unity.

For the Zn/air battery tests, a homemade mini battery was built as presented in Figure S1. The battery case was constructed using an acrylic block (2 × 2 cm<sup>2</sup>) containing a cavity (1.5 mL in volume) to store the supporting KOH aqueous electrolyte solution (6.0 mol L<sup>-1</sup>) and a zinc foil (1.0 × 1.5 cm<sup>2</sup>) which was used as anode. The battery was completed by connecting the cathode, produced as a gas diffusion electrode using a carbon cloth (Panex 30 PW03) which was attached to the battery case by a stainless-steel screen. The stainless-steel screen served also as current collector. The gas diffusion electrodes were manufactured by depositing a catalytic layer into a 1.54 cm<sup>2</sup> delimited area of a carbon micro porous layer previously deposited on the carbon cloth substrate following the methodology described by Paganin et al. [20]. The catalytic layer was prepared by mixing the catalyst (3.08 mg) with of a Nafion® solution (3 drops, 1:10 in isopropanol) and isopropanol (5 drops) and brushing the dispersion on the surface of the micro porous layer. The gas diffusion electrode is then transferred to an oven and submitted to a thermal treatment at 80 °C for 2 h under N<sub>2</sub> atmosphere. The battery was evaluated by polarization curves obtained at 1 mV s<sup>-1</sup> and by electrochemical impedance spectroscopy measurements. The measurements were conducted at room temperature using a Metrohm Autolab (BV, Netherlands) potentiostat, model PGSTAT 30 equipped with a FRA2 μAutolab Type III module controlled by the N.O.V.A. v1.11 software. The impedance spectra were analyzed using the EIS Spectrum Analyser v1.0 software [21].

### 3. Results and discussions

#### 3.1. Physical characterizations

Powder XRD and Rietveld refinement were used to evaluate the crystallographic structure and estimate the presence and positions of ions and water inside the tunnel, Fig. 1. Cryptomelane has a tetragonal crystal structure with space group I 4/m (87) and all doped MnO<sub>2</sub> samples showed diffraction peaks related to this crystallographic structure (ICSD: 44–141). Standard XRD pattern has  $a = b = 9.82303 \text{ \AA}$  and  $c = 2.853725 \text{ \AA}$ , which gives a cell volume of 275.3614 Å<sup>3</sup>. The pure α-MnO<sub>2</sub> CIF file used in the Rietveld refinement cannot fit the observed XRD pattern due to the presence of matter inside the tunnel. To precisely locate the crystallographic position of cations and water within the α-MnO<sub>2</sub> unit cell, the Fourier maps plots for the observed structure factor ( $F_{\text{obs}}$ ) obtained using the doped structures model (CIF files) and the difference of  $F_{\text{obs}}$  and the calculated structure factor ( $F_{\text{cal}}$ ) using the pure α-MnO<sub>2</sub> structure as a model were performed, Fig. 1A. As all three α-MnO<sub>2</sub> samples showed similar water and ions positions, only the xK<sup>+</sup>.yH<sub>2</sub>O. MnO<sub>2</sub> result is discussed in detail and the other samples results are showed in the supporting information. Fourier maps for XRD results display the scattering densities that are related to the electron densities of atoms located within the unit cell, which is also related to the structure factor ( $F_{(x,y,z)}$ ) according to Eqs. (1)–(3). After the refinement using the pure α-MnO<sub>2</sub>, without the K<sup>+</sup> and H<sub>2</sub>O content, difference maps ( $F_{\text{obs}} - F_{\text{cal}}$ ) were obtained and used to locate the cations inside the unit cell. This map can be used to increase the response of atoms positions with low site occupancy ( $f_i$ ), which could decrease the structure factor  $F$  for a reflection ( $hkl$ ), according to Eq. (1). Therefore, two atomic positions were observed, the first on the center of the (2 × 2) tunnel (Wyckoff 2a positions), and the second on the center of the  $ab$ -facet (Wyckoff 2b positions), which is also located inside the tunnel. The former was ascribed to K<sup>+</sup> ions and

the latter for the water molecules inside the tunnel, in agreement with some results in literature for other cations doped α-MnO<sub>2</sub> [22,23]. Therefore, new crystallographic structures updated with this ions and water positions were used to perform Rietveld refinement of doped α-MnO<sub>2</sub> XRD data.

$$F_{hkl} = \sum_{j=1}^m N_j f_j \exp[2\pi i(hx_j + ky_j + lz_j)] \quad (1)$$

$$\rho_{(x,y,z)} = \frac{1}{V} \sum_h \sum_k \sum_l F_{(x,y,z)} \exp[-2\pi i(hx + ky + lz)] \quad (2)$$

$$\begin{aligned} \rho(x, y, z, )_{\text{exp}} - \rho(x, y, z, )_{\text{model}} \\ = \sum_{hkl} (F_{\text{obs}} - F_{\text{calc}})_{hkl} \cos 2\pi(hx + ky + lz + \Phi_{\text{calc-hkl}}) \end{aligned} \quad (3)$$

Rietveld refinement of XRD results for doped α-MnO<sub>2</sub> structures are summarized in Table 1. All three samples showed good R-factors and goodness of fit (GOF) for their respective crystallographic models (CIF files), which supports the formation of doped α-MnO<sub>2</sub> samples. The schematic representations of α-MnO<sub>2</sub> (K<sup>+</sup>, Bi<sup>3+</sup>, and Ce<sup>4+</sup>) structures are presented in the inset of the respective XRD patterns showing the cations (purple, brown, and yellow colors for K<sup>+</sup>, Bi<sup>3+</sup>, and Ce<sup>4+</sup>, respectively) and water (half red and white atoms) positions as well as Mn–O octahedral (green surface) structure within the unit cell, being four unit cells displayed to better represent the nanorods structure by the [001] direction perspective, which is parallel to the (2 × 2) tunnel direction. As the nanorods possess an anisotropic shape, both Stephens and the spherical harmonics models for preferred orientation and anisotropic line broadening from TOPAS were used to fit the XRD data and accurately represent our results. The peak around 65.4° (20) from the (002) plane, direction of rods growth, is the mostly affected by the preferred orientation. The peak around 37.5°, associated with (211) plane, which have a multiplicity of 8, is the most intense peak that is also related to rods preferred orientation caused by the anisotropic shape. The first four peaks below 35°, correspond to (110), (020), (220), and (130) planes, have a strong relationship with the tunnel occupancy by cations and water, and the occupancy factor for each refinement were properly adjusted to fit the XRD intensities and ascertain the quantity of cations and water inside the tunnel. Concerning the atomic radius series, where K<sup>+</sup> > Bi<sup>3+</sup> > Ce<sup>4+</sup>, there was no direct correlation relating the unit cell volume with cations dimensions comparing the three samples, probably due to the different  $f_i$  observed for doped α-MnO<sub>2</sub> samples ( $f_{K^{+2}} = 0.017$ ,  $f_{Ce^{+4}} = 0.0061$ ,  $f_{Bi^{+3}} = 0.00039$ ). The water  $f_i$  for all three samples were close to 1, indicating that the (2 × 2) tunnel is fully filled with H<sub>2</sub>O molecules.

Fig. 2 shows the XPS spectra of all doped α-MnO<sub>2</sub> samples featuring the Mn 2p and O 1s spectra along with the cations K 1s, Bi 4f, and Ce 3d spectra for their respective samples. The survey spectrum for each sample showed only carbon as contaminant and no substantial presence of other impurities, Fig. S3. The Mn 2p spectra were fitted with two Voigt profile (Gaussian-Lorentzian) peaks of varying full width at half maximum (FWHM) for both doublet 2p<sub>3/2</sub> (p1 and p2) and 2p<sub>1/2</sub> (p3 and p4) peaks, the area ratio between correlated p<sub>1/2</sub> and p<sub>3/2</sub> peaks were constrained to have 1:2 for p1/p3 and p2/p4, and the magnitude of peak splitting was also constrained to rely around 11.1–11.8 eV. The presence of two chemical environments for Mn<sup>4+</sup> could be ascribed to the presence of the bulk MnO<sub>6</sub> octahedra (O–Mn–O), p1 (~642.3 eV) and p3 (~644.1 eV) peaks, and the surface environment that could present the O–Mn–OH structure, p2 (~653.5 eV) and p4 (~655.1 eV) peaks. A small amount of Mn<sup>3+</sup> could also be present probably due to the cations inside the tunnel, which can induce the reduction of Mn<sup>4+</sup> to Mn<sup>3+</sup> to keep charge neutrality, and oxygen vacancies that could also contribute to Mn<sup>3+</sup> formation [24]. However, the Mn<sup>3+</sup> 2p<sub>3/2</sub> peak should be located around 641 eV, and it was not observed for the samples analyzed [25]. Then, the Mn 3s XPS region was used to analyze the oxidation

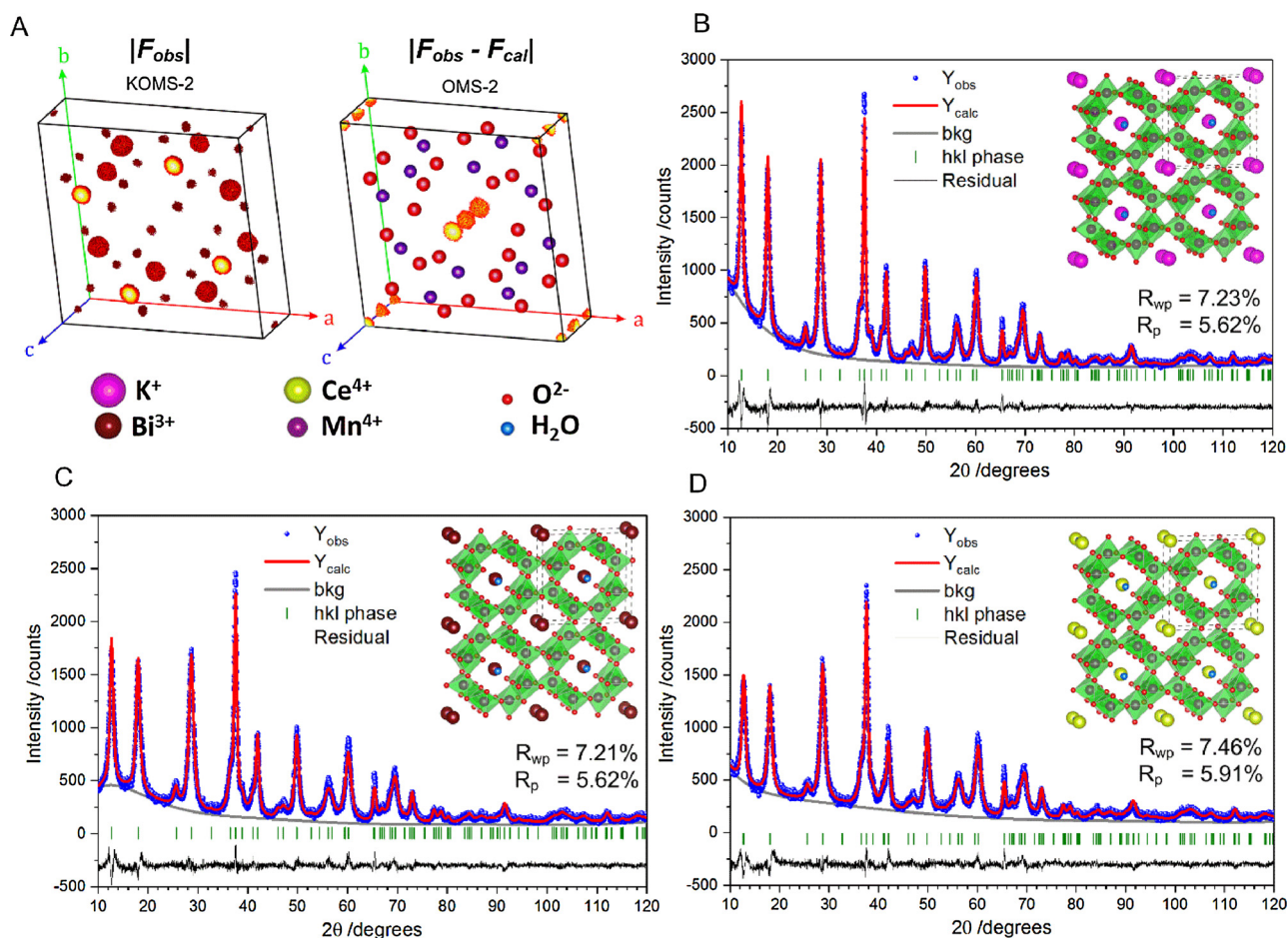


**Fig. 1.** (A)  $|F_{obs}|$  and  $|F_{obs} - F_{calc}|$  Fourier maps for  $xK^+ \cdot yH_2O \cdot MnO_2$  (KOMS-2) and pure  $MnO_2$ , respectively, used to determine the dopants and water molecules positions inside the  $\alpha$ - $MnO_2$  structures; Rietveld refinement of powder XRD patterns for doped  $\alpha$ - $MnO_2$  samples (B)  $xK^+ \cdot yH_2O \cdot MnO_2$ , (C)  $xBi^{3+} \cdot yH_2O \cdot MnO_2$ , and (D)  $xCe^{4+} \cdot yH_2O \cdot MnO_2$ . The insets show the final structure determination for the doped  $\alpha$ - $MnO_2$  samples showing the position of  $K^+$ ,  $Bi^{3+}$  and  $Ce^{4+}$  cations along with the  $H_2O$  inside the  $(2 \times 2)$  tunnel.

**Table 1**

Rietveld refinement results for doped  $\alpha$ - $MnO_2$  ( $K^+$ ,  $Bi^{3+}$ , and  $Ce^{4+}$ ) samples.

Chemical formula	$xK^+ \cdot 1H_2O \cdot MnO_2$	$xBi^{3+} \cdot 1H_2O \cdot MnO_2$	$xCe^{4+} \cdot 1H_2O \cdot MnO_2$
Crystal System	tetragonal	tetragonal	tetragonal
Space Group	$I 4/m (87)$	$I 4/m (87)$	$I 4/m (87)$
Z formula unit	8	8	8
a (Å) = b (Å)	9.8218	9.8276	9.8356
c (Å)	2.8536	2.8520	2.8523
V (Å <sup>3</sup> )	275.28	275.46	275.94
Density (g cm <sup>-3</sup> )	4.40	4.42	4.39
Rwp (%)	7.23	7.21	7.46
Rp (%)	5.62	5.62	5.91
Rexp (%)	5.59	5.60	5.37
GOF	1.29	1.29	1.39

state of manganese as the energy separation between peaks have a linear relationship between  $Mn^{3+}$  (5.5 eV) and  $Mn^{4+}$  (4.8 eV), Fig. S4. The difference in peaks splitting for KOMS-2 was 5.1 eV indicating a partial reduction of  $Mn^{4+}$  and the presence of  $Mn^{3+}$  in the sample structure. The O 1s XPS spectra for KOMS-2 and BiOMS-2 showed similar behavior indicating the presence of three peaks assigned to  $O^{2-}$  (529.7 eV),  $OH^-$  (531.3 eV), and  $H_2O$  (532.7 eV) related to oxygens from bulk  $MnO_6$ , surface M-OH, and water, respectively, in agreement with the presence of two Mn chemical environment. However, differently than KOMS-2 and BiOMS-2 samples, the CeOMS-2 XPS spectra showed an increased  $OH^-$  and  $H_2O$  signals intensity compared to  $O^{2-}$  peak, which indicates that the acid treatment to keep  $Ce^{4+}$  cations

soluble also inflicted structural damage to OMS nanorods, increasing the presence of Mn-OH and the water adsorbed onto the nanorods surfaces. Besides the XRD data, the presence of the three dopants in OMS-2 structures was evaluated observing the XPS region for each dopant. The K 2p spectra, near the C 1s peaks, showed the  $2p_{3/2}$  (295.7 eV) and  $2p_{1/2}$  (298.3 eV) peaks.  $Bi^{3+}$  4f spectrum showed two doublets  $4f_{7/2}$  (159.4 eV) and  $4f_{5/2}$  (164.8 eV) peaks and a separated spin-orbit of 5.4 eV, as expected for bismuth. Cerium 3d spectrum presents the  $2d_{5/2}$  and  $2d_{3/2}$  peaks fitted using both  $Ce^{4+}$  and  $Ce^{3+}$  species, which were labeled using Burroughs's nomenclature. Therefore, XPS and XRD results for doped samples showed the existence of the  $\alpha$ - $MnO_2$  structure having minor quantity of defects, as observed by



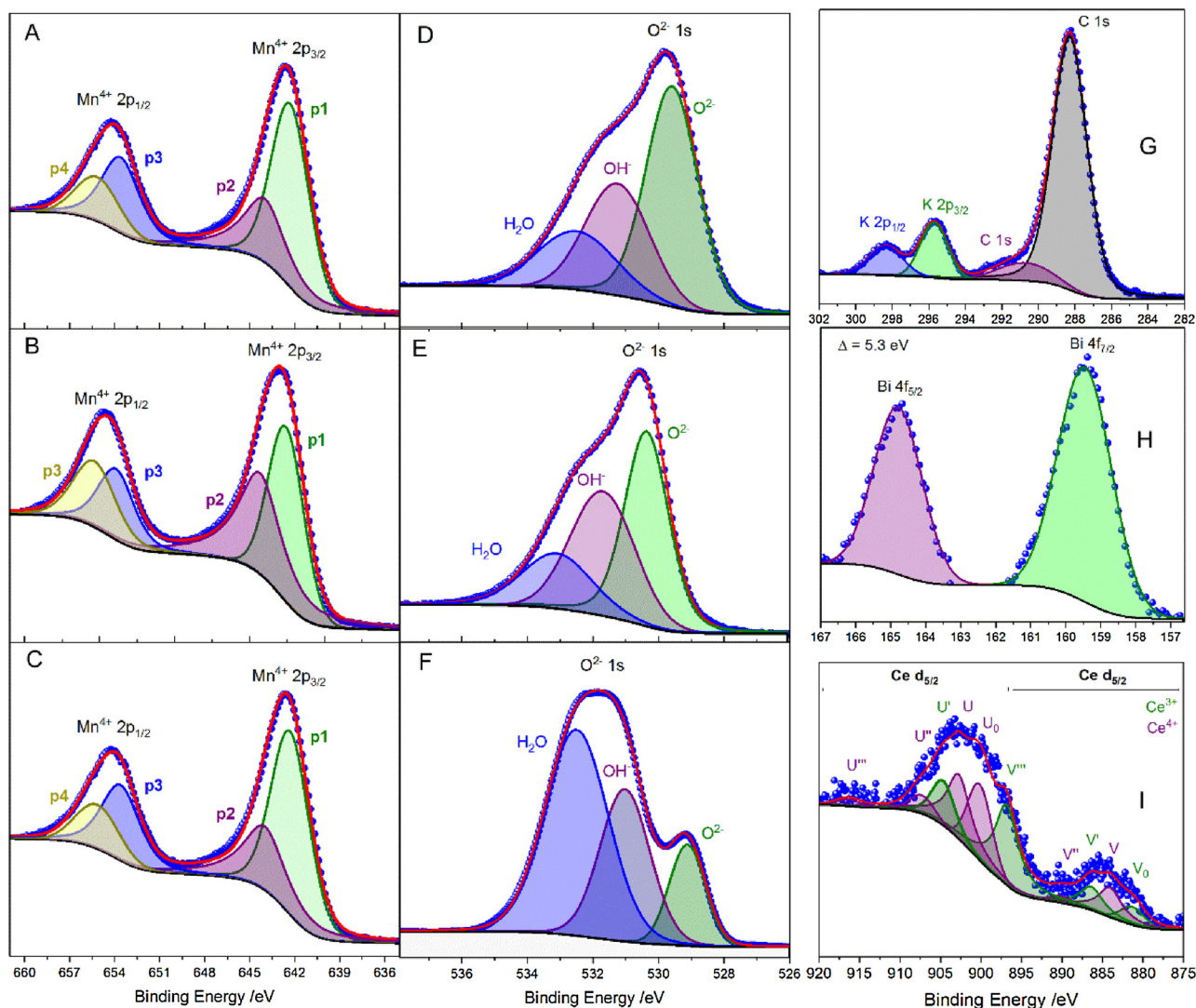


Fig. 2. X ray photoelectron spectroscopy (XPS) of (A–C) Mn 2p, (D–F) O 1s and (G–I) K 2p, Bi 4f and Ce 3d regions for KOMS-2, BiOMS-2, and CeOMS-2, respectively.

the presence of  $\text{Mn}^{3+}$ , except the CeOMS-2 that showed higher Mn-OH structures and the presence of mixed valence Ce cations.

UV–vis and Diffuse Reflectance Spectroscopy (DRS) were used to analyze the  $E_{\text{BG}}$  of  $\alpha\text{-MnO}_2$  samples using the Tauc and Kubelka Munk plot, respectively, Fig. 3. UV–vis spectra for all three samples showed a broad absorption band centered around 400 nm with an inflection point near 500 nm (2.48 eV) that was used to draw the tangent line in the Tauc plot. The observed  $E_{\text{BG}}$  for KOMS-2, BiOMS-2, and CeOMS-2 were 2.04, 1.97, and 1.93 eV, respectively, using an exponent  $n$  equal  $\frac{1}{2}$  attributed to a direct allowed transition. Although DFT calculations in the literature for pure cryptomelane claim that bulk  $E_{\text{BG}}$  is around 2.7 eV with indirect band structure, all three samples showed better straight-line fit for the absorption tail region, near the band edge, using  $n$  equal  $\frac{1}{2}$  instead of 2. Similarly, DRS spectra was obtained and the reflectance ( $R_{\infty}$ ) was converted to  $F(R_{\infty})$  using the well-known Kubelka-Munk function. As  $F(R_{\infty})$  is proportional to the absorption coefficient  $\alpha$ , the Kubelka-Munk plot,  $(F(R_{\infty})h\nu)^2$  vs.  $h\nu$ , were also used to determine the optical band gap through reflectance experiments. The same trend was observed being the  $E_{\text{BG}}$  for BiOMS-2 (1.54 eV) and CeOMS-2 (1.88 eV) smaller than the KOMS-2 (2.01 eV). The indirect allowed  $E_{\text{BG}}$  were also estimated for KOMS-2, BiOMS-2, and CeOMS-2 using both Tauc plot and Kubelka-Munk Plot, Fig. S5 and Table S1. Whereas  $(F(R_{\infty})h\nu)^{1/2}$  plot showed the same tendency with KOMS-2 presenting higher  $E_{\text{BG}}$ , the  $(\alpha h\nu)^{1/2}$  plot showed unusual results with BiOMS-2 presenting slightly

higher  $E_{\text{BG}}$  (2.00 eV) than KOMS-2 (1.93 eV) and BiOMS-2 (1.82 eV). The optical band gap with indirect transition are not trivial to be determined using Tauc and Kubelka Munk plot due to the second linearity region at lower  $h\nu$  attributed to phonon absorption. Observing the absorption tail region in UV–vis spectra around 620 nm (~2.0 eV) it is expected that  $E_{\text{BG}}$  relies nearby this absorption threshold. It is important to point out that typically KOMS-2 showed the highest  $E_{\text{BG}}$  compared to other doped samples, indicating that the presence of  $\text{Bi}^{3+}$  and  $\text{Ce}^{4+}$  in the  $(2 \times 2)$  tunnel can tune electronic behavior of  $\alpha\text{-MnO}_2$  structures. Variations in valence of manganese cations and the presence of surface states could also change the electronic configuration of cryptomelane nanorods [26].

$$(h\nu\alpha)^{1/n} = A(h\nu - E_g) \quad (4)$$

$$(h\nu F(R_{\infty}))^{1/n} = A(h\nu - E_g) \quad (5)$$

$$F(R_{\infty}) \propto \alpha = \frac{(1 - R_{\infty})^2}{2R_{\infty}} \quad (6)$$

Fig. 4A–C presents low-magnification TEM images of KOMS-2, BiOMS-2 and CeOMS-2 catalysts. Nanorod structures were formed in all three samples with an average diameter of ~10 nm and length ranging from ~25 nm to ~500 nm. The HRTEM micrograph presented in Fig. 4D is typical for all three samples and shows a highly crystalline KOMS-2 material evidenced by the long-range order of crystallinity from the

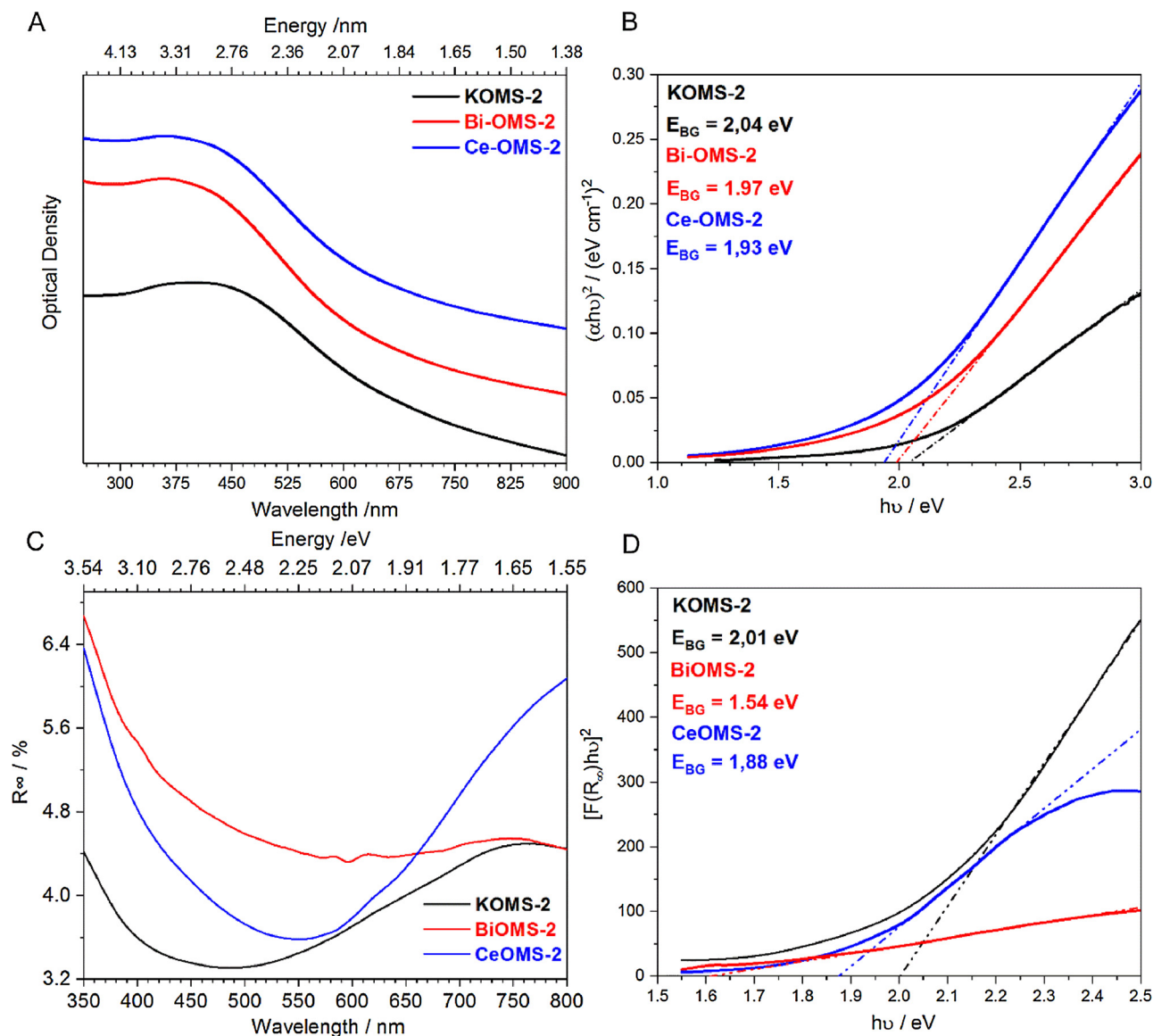


**Fig. 3.** (A) UV-vis spectra, (B) Tauc plot  $(\alpha h\nu)^2$  (direct band gap), (C) Diffuse Reflectance Spectra, and (D) Kubelka Munk plot  $[F(R_\infty)h\nu]^2$  (direct band gap) for  $\alpha$ -MnO<sub>2</sub>-doped samples used to evaluate the optical band gap energy ( $E_{BG}$ ).

well-formed lattice fringes with interplanar distance of 4.9 Å, corresponding to the (020) plane. Nanorods presented the direction of growth along the [001] direction that is parallel to the c-axis and the (2 × 2) tunnel longitude, as showed in the insets of Fig. 1. This is consistent with the preferred orientation observed in the XRD results and confirmed by the Rietveld refinement. Similar HRTEM micrographs were also obtained for the other materials, Fig. S6. Clearly, the acid treatment necessary to produce CeOMS-2 resulted in nanorods with rougher surfaces, Fig. S6A, when compared with BiOMS-2 and KOMS-2. This result has some implications in the electrodes performances as will be discussed latter in the electrochemical characterization. The selected area electron diffraction (SAED) result for BiOMS-2 nanorods in Fig. 4E showed the diffraction rings indexed to (002), (141), (121), (130), (110), (020), (220), (031) and (251) planes, indicating a highly crystalline material consistent with the XRD and HRTEM results for the space group *I* 4/*m* ( $\alpha$ -MnO<sub>2</sub>).

### 3.2. Electrochemical characterization of the catalysts

#### 3.2.1. Cyclic voltammetry

The cyclic voltammetric response of KOMS-2, BiOMS-2 and CeOMS-

2 obtained at a scan rate of 10 mV s<sup>-1</sup> in an aqueous KOH solution (1.0 mol L<sup>-1</sup>) saturated with N<sub>2</sub> and in room temperature is presented in Fig. 5. The cyclic voltammetric profiles obtained are typical of MnO<sub>2</sub> characterized by a series of redox peaks associated with the oxidation and reduction of manganese dioxide as widely discussed in the literature [19,27–30]. Clearly the cyclic voltammogram of Bi and Ce doped catalysts present more features and better defined voltammetric peaks in the potential range studied compared with KOMS-2. Additionally, the cyclic voltammetric profile of KOMS-2 is considerably inclined indicating a significant ohmic effect associated with the semiconducting nature with wide band gap of this material. The results presented in Fig. 5 indicates that Bi and CeOMS-2 present improved electronic conduction compared to KOMS-2 in agreement with the narrow  $E_{BG}$  found for these materials using diffuse reflectance measurements, Fig. 3B and D.

#### 3.2.2. Electroreduction of oxygen

Hydrodynamic polarization curves were obtained using the RDE technique to evaluate the electrocatalytic performance of MnO<sub>2</sub> based catalysts. Fig. 6A shows the quasi-steady state polarization curves for the ORR on KOMS-2, BiOMS-2 and CeOMS-2 catalysts, which was



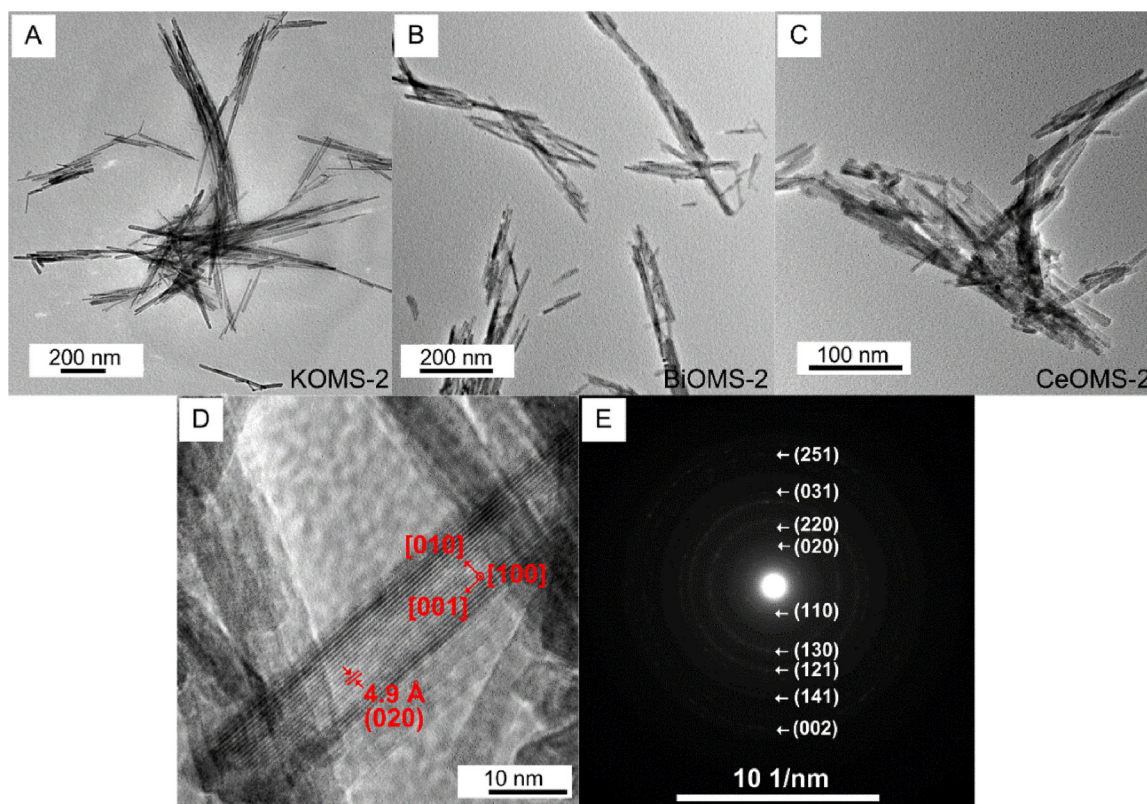


Fig. 4. TEM micrographs: (A–C) low-magnification images of KOMS-2, BiOMS-2 and CeOMS-2 catalysts; (D) HRTEM image of KOMS-2 nanorod showing lattice fringes of 4.9 Å corresponding to (020) KOMS-2 planes; (E) SAED along with the index of BiOMS-2 nanorods.

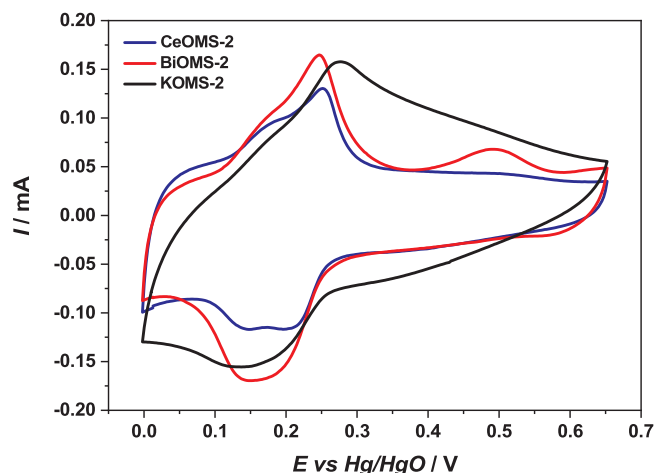


Fig. 5. Cyclic voltammograms of KOMS-2, BiOMS-2 and CeOMS-2, obtained at a scan rate of  $10 \text{ mV s}^{-1}$  in an aqueous KOH solution ( $1.0 \text{ mol L}^{-1}$ ) saturated with  $\text{N}_2$ .

obtained at 900 rpm of electrode rotation rate ( $\omega$ ),  $3 \text{ mV s}^{-1}$  of potential scan rate ( $\nu$ ) and using an aqueous KOH solution ( $1.0 \text{ mol L}^{-1}$ ) saturated with  $\text{O}_2$ . Polarization curves for a commercial Pt/C 20 wt.% (Etek) catalyst and a carbon powder electrode (Printex 6L) were included in the same graph to compare the ORR responses with those obtained for doped OMS-2 materials. These reference materials catalyze the ORR in alkaline solutions through the direct ( $4e^-$  transferred per  $\text{O}_2$  molecule) and peroxide ( $2e^-$  transferred per  $\text{O}_2$  molecule) mechanisms respectively. As already suggested by the CV experiments, clearly doping  $\text{MnO}_2$  with Bi and Ce decrease the oxide material resistivity. The polarization curve for the ORR on KOMS-2 is remarkably affected by an ohmic contribution associated with the low electron conductance

presented by this material, which can be seen by the inclination of the I vs E response. The curve is very inclined, without a well-defined diffusional plateau, differently from the behavior presented by doped and standard catalysts.

The most remarkable aspect of the polarization curves presented in Fig. 6A is the catalytic performance of the BiOMS-2 and CeOMS-2 materials. An appropriate parameter to evaluate their performances is by comparing the half-wave potential values in the kinetically controlled region for the catalysts studied, which is situated between the diffusional plateau and the kinetically controlled region. The most active catalysts are that one presenting higher half-wave potential values. Using this indicator, Fig. 6A reveals that the catalytic performances for the ORR follow the sequence  $\text{CeOMS-2} > \text{BiOMS-2} > \text{Pt/C 20 wt. \%} > \text{Printex 6L} > \text{KOMS-2}$ . Considering that the kinetically controlled potential range is the most important one for practical applications, the result presented in Fig. 6 is extremely significant. It means in practice that CeOMS-2 and BiOMS-2 can advantageously replace platinum as cathode catalysts in metal-air batteries and alkaline fuel cells, a subject that has been exhaustively studied in electrocatalysis for energy conversion devices. The results are even more important considering that the catalysts are carbon free and consequently are eligible to act as bifunctional catalysts in the cathode of alkaline metal/air batteries and fuel cells.

Among the two cations doped  $\text{MnO}_2$  catalysts studied, CeOMS-2 was the most active for the ORR. Comparing the TEM images presented in Fig. S6A and B for CeOMS-2 and BiOMS-2 respectively, the CeOMS-2 nanorods have a much rougher surface. It is proposed in the literature [8,19,27,29,30] that the active sites for the ORR on  $\text{MnO}_2$  based catalysts is the trivalent cation  $\text{Mn}^{3+}$ , more specifically, the  $\text{MnOOH}$ , as exemplified for the peroxide two-electron reduction pathway as follows:



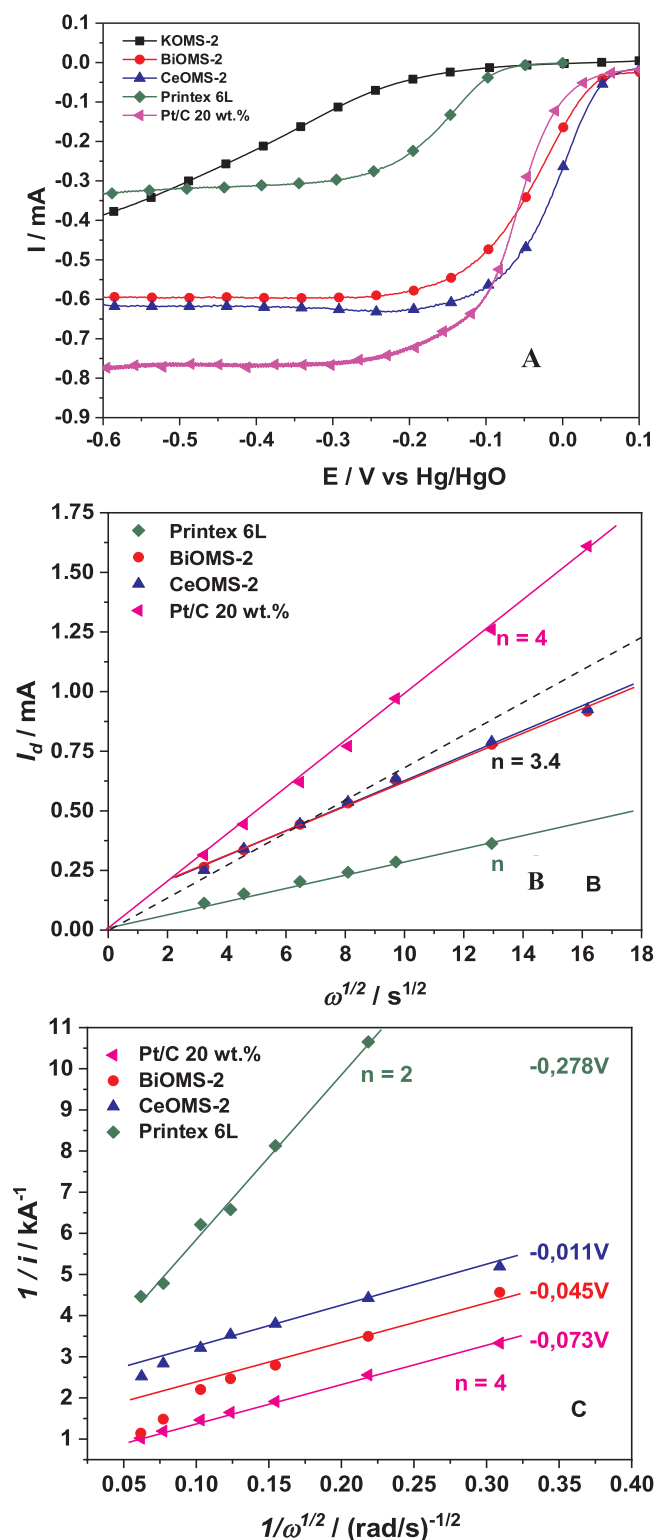


**Fig. 6.** (A) Polarization curves for the oxygen reduction reaction on different electrocatalysts in oxygen saturated KOH aqueous solution (1.0 mol L<sup>-1</sup>),  $\omega = 900$  rpm;  $\nu = 3$  mV s<sup>-1</sup>; (B) Levich plots and (C) Koutecky-Levich plots for the ORR on different electrocatalysts; (■) KOMS-2 (0.25 mg<sub>KOMS-2</sub> cm<sup>-2</sup>); (◆) Printex 6L (0.25 mg<sub>Printex 6L</sub> cm<sup>-2</sup>); (●) BiOMS-2 (0.25 mg<sub>BiOMS-2</sub> cm<sup>-2</sup>); (▲) CeOMS-2 0.25 (0.25 mg<sub>CeOMS-2</sub> cm<sup>-2</sup>); (▼) Pt/C 20 wt.% (Etek) (0.05 mg<sub>Pt/C</sub> cm<sup>-2</sup>).



Considering that the MnOOH generated in reaction (1) has almost the same structure of the MnO<sub>2</sub> precursor [19], nanorods with rougher surfaces, as in the case of CeOMS-2 would certainly result in a material with a higher Mn<sup>3+</sup> surface concentration due to the higher active surface area, which explain satisfactorily the superior catalytic activity presented by this material in Fig. 6A when compared with BiOMS-2.

The evaluation of the reaction mechanism for the oxygen reduction on the different catalysts systems may be performed by analyzing the mass diffusion current values ( $i_d$ ) in the polarization curves presented in Fig. 6A. The  $i_d$  value is directly proportional to the number of electrons transferred per oxygen molecule ( $n$ ). Comparing the results obtained for Pt/C (the reference material for the 4e<sup>-</sup> pathway), BiOMS-2 and CeOMS-2, the  $i_d$  values for the oxides are lower than that obtained for Pt/C. This is an indication that at some extension, hydrogen peroxide is formed as product when the ORR is catalyzed by BiOMS-2 or CeOMS-2. In this aspect, this result is similar to that obtained for MnO<sub>2</sub> based catalysts as already discussed in the literature [19,27,29,30]. The Levich equation [31] below predicts how  $i_d$  relates with  $n$  and how it can be used to estimate numerically this parameter:

$$i_d = (0.62)nFAD^{2/3}\nu^{-1/6}C^*\omega^{1/2} \quad (7)$$

where  $i_d$  is the mass diffusion limiting current (or Levich current, A),  $n$  the number of electrons transferred in the reaction,  $F$  the Faraday constant (96,485 C mol<sup>-1</sup>),  $A$  the electrode geometric area (0.2475 cm<sup>2</sup>),  $D$  the diffusion coefficient of oxygen in KOH 1.0 mol L<sup>-1</sup> (1.9 10<sup>-5</sup> cm<sup>2</sup> s<sup>-1</sup>),  $\omega$  the angular rotation rate of the electrodes (rad s<sup>-1</sup>),  $\nu$  the kinematic viscosity of KOH 1.0 mol L<sup>-1</sup> (1.0 10<sup>-2</sup> cm<sup>2</sup> s<sup>-1</sup>), and  $C^*$  the oxygen solubility in KOH 1.0 mol L<sup>-1</sup> (1.2 10<sup>-6</sup> mol cm<sup>-3</sup>).

Fig. 6B presents the Levich curves ( $i_d$  vs  $\omega^{1/2}$ ) for the reference catalysts, Pt/C 20 wt.% and carbon powder, as well for BiOMS-2 and CeOMS-2 samples. The number of electrons related to the oxygen reduction reaction were calculated from the slopes of the Levich curves that were obtained from the polarization data from different electrode rotation rates. The constants values in the Levich equation were obtained from the literature [32,33]. For the ORR on Pt/C 20 wt.% and on carbon  $n$  is 4 and 2 respectively, as expected. For the cations doped MnO<sub>2</sub> based catalysts, the number of electrons exchanged estimated lies between 2 and 4 as suggested by the polarization curves presented in Fig. 6A. This result indicates that the mechanism of ORR on MnO<sub>2</sub> catalysts involves the formation of peroxide as intermediate or final product. Similar results have been obtained for the ORR on carbon supported MnO<sub>2</sub> on previous works [19,27,29,30]. In fact, analyzing carefully the Levich curves for BiOMS-2 and CeOMS-2 a curvature can be clearly observed, and the linear coefficient is not zero. The linear coefficient for a set of experimental data that satisfies the Levich equation must be zero and this is the case for Pt/C 20 wt.% and for the carbon catalyst. For the oxide catalysts the Levich curves apparently deviates from the normal behavior expected. This effect is related with the oxygen recycling formed by the chemical decomposition of hydrogen peroxide, a product from the oxygen reduction, on the oxide catalyst surface.

A black dashed line is displayed in Fig. 6B to compare with the BiOMS-2 (red line) and CeOMS-2 (blue) curves which shows that at low electrode rotation rates the apparent number of electrons exchanged is higher than that calculated from slope of the curve. At lower rotation rates, the residence time of hydrogen peroxide near the catalyst surface is higher and a considerable amount of peroxide is decomposed to oxygen. A part of the oxygen recycled can react again on the catalyst surface generating peroxide and therefore the apparent number of electrons is close to 4. For higher electrode rotation rates, a greater part of the peroxide formed is faster transported to bulk of the solution and the number of electrons exchanged is lower than at that lower electrode



rotation rates. Such kind of effect has been observed by Calvo et al. [34] for the oxygen reduction reaction on  $\text{Fe}_3\text{O}_4$  electrodes. For this system, the Koutecky-Levich plots [31] are curved as result of the oxygen recycling from the hydrogen peroxide decomposition on the oxide surface. In Fig. 6C is presented the Koutecky-Levich plots for the catalysts studied. For BiOMS-2 and CeOMS-2 the Koutecky-Levich plots are clearly curved as in the case of the iron oxide electrodes in Calvo's work [34]. This result indicates that on the  $\text{MnO}_2$  based catalysts, the ORR is catalyzed by the peroxide mechanism, followed by chemical decomposition and subsequent reduction of the regenerated  $\text{O}_2$  (oxygen recycling), but based on the studies of catalysts stabilities and analyzes of materials after extended used, which will be presented latter in this paper, certainly the direct pathway involving  $4e^-$  must be considered. Considering the corrosive nature of hydrogen peroxide, it would be expected that a severe degradation of catalyst performance associated with catalyst corrosion should be obtained after extended use. However, none of these situations have been observed either for BiOMS-2 or CeOMS-2. This result suggests the existence of parallel pathways of 2 (with oxygen recycling) and 4 electrons pathway, in a higher extension for the direct pathway. Hydrogen peroxide is formed in some extension, but in a concentration not high enough to result in damages to the catalysts surfaces.

For energy conversion devices the best catalysts for the ORR are that capable to catalyze the reaction through the  $4e^-$  pathway (peroxide mechanism). In this aspect, the use of BiOMS-2 and CeOMS-2 are very favorable, because although the ORR proceeds in some extension through the peroxide mechanism, the utilization of a stagnated solution as in the case of metal-air batteries implies oxygen recycling and, in this case, the number of electrons exchanged is close to 4, the ideal case.

### 3.2.3. Oxygen evolution reaction (OER)

Besides the ORR experiments, doped  $\text{MnO}_2$  based catalysts were evaluated to operate as bifunctional cathode catalysts by also testing their performance for the OER. For this purpose, polarization curves at  $3 \text{ mV s}^{-1}$  in KOH aqueous solution ( $1.0 \text{ mol L}^{-1}$ ) saturated with  $\text{N}_2$  were obtained for each catalyst studied, Fig. 7. For clarity of presentation and to facilitate the comparison with the experimental data available in the literature, the overpotential of the OER is presented in the top x-axis and the potential values were converted to the reversible hydrogen electrode reference scale. For the same reason, the plots were

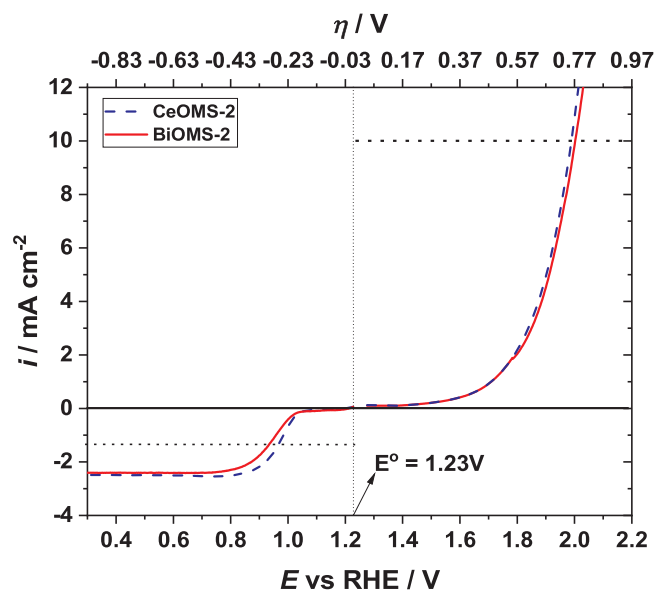


Fig. 7. Polarization curves for the OER ( $\text{N}_2$  saturated solution) and ORR ( $\text{O}_2$  saturated solution) on (---) BiOMS-2 ( $0.25 \text{ mg}_{\text{BiOMS-2}} \text{ cm}^{-2}$ ) and (—) CeOMS-2 ( $0.25 \text{ mg}_{\text{CeOMS-2}} \text{ cm}^{-2}$ ) at  $3 \text{ mV s}^{-1}$  in KOH aqueous solution ( $1.0 \text{ mol L}^{-1}$ ).

constructed using current density in the y-axis by normalizing the current values obtained experimentally by the geometric area of the working electrodes, i.e.  $0.2475 \text{ cm}^2$ . Clearly, BiOMS-2 and CeOMS-2 have almost identical performances for the OER, the same tendency observed in the ORR presented above. A convention used in the literature to measure the activity for the OER of a catalyst is by evaluating the potential required to oxidized water at  $10 \text{ mA cm}^{-2}$ , or simply by estimating the reaction overpotential at this current density [35].

The overpotentials for the OER on the different catalysts at  $10 \text{ mA cm}^{-2}$  were estimated as  $\eta_{\text{BiOMS-2}} = 0.78 \text{ V}$  and  $\eta_{\text{CeOMS-2}} = 0.76 \text{ V}$ . Reference overpotential values for the OER on  $\text{MnO}_2$  reported in the literature range from 0.400 to 0.540 V depending on the oxide structure and other factors [36–38]. Manganese dioxide has been considered a reasonable catalyst for the OER owing to its low conductivity. Improvements have been obtained by mixing some conductive and active OER catalyst such as  $\text{RuO}_2$  [35]. In the present case, the overpotential for the OER is higher than those observed in the literature as no other catalyst was added to the system. Nevertheless, the very good performance obtained using doped OMS-2 materials as catalysts for the ORR compensate the lower performance for the OER. The most adequate parameter to evaluate the overall performance of a bifunctional electrocatalyst for the oxygen reactions (reduction and evolution) is by measuring the difference ( $\Delta E$ ) between the potential at  $10 \text{ mA cm}^{-2}$  for the OER and the half-wave potential for the ORR [39] as indicated in Fig. 7. The values of  $\Delta E_{\text{BiOMS-2}} = 1.07 \text{ V}$  and  $\Delta E_{\text{CeOMS-2}} = 1.02 \text{ V}$  are very close to that obtained when reference materials are used as catalysts for the OER, such as Ir ( $\Delta E_{\text{Ir}} = 0.92 \text{ V}$ ) which has also an electrocatalytic performance for the ORR close to that observed for carbon supported  $\text{MnO}_2$  catalysts. Therefore, both ORR and OER results compared to typical results for reference materials, as discussed above, indicates that CeOMS-2 and BiOMS-2 are adequate materials to be used as bifunctional catalysts for the cathode of metal-air batteries and alkaline fuel cells.

### 3.2.4. Zn/air mini battery tests

The electrocatalytic performance of  $\text{MnO}_2$  based catalysts was further evaluated using a home-made primary Zn/Air mini-battery assembled as presented in Fig. S1. The tests were conducted at room temperature using atmospheric air as oxidant instead of pure oxygen. Fig. 8 presents the results obtained using the catalysts studied previously in the semi-cell configuration. A conventional carbon supported  $\text{MnO}_2$  catalyst (50 wt.%), produced by the mixture of KOMS-2 catalyst previously synthesized with Vulcan XC-72 carbon powder, was used for comparison purposes.

The performances were almost the same as that observed in the hydrodynamic experiments, section above for the ORR. The battery assembled with KOMS-2 catalyst in the cathode presented the poorest performance, with a peak power density of  $110 \mu\text{W cm}^{-2}$  at  $125 \mu\text{A cm}^{-2}$ . On the other hand, when the battery was assembled with the cations doped  $\text{MnO}_2$  as cathode catalysts much higher performances were obtained. CeOMS-2 presented the best overall performance with a power density of  $45 \text{ mW cm}^{-2}$  at  $120 \text{ mA cm}^{-2}$ , better than the conventional OMS-2/C 50 wt.% catalyst ( $40 \text{ mW cm}^{-2}$  at  $100 \text{ mA cm}^{-2}$ ) and better than BiOMS-2 ( $30 \text{ mW cm}^{-2}$  at  $100 \text{ mA cm}^{-2}$ ). This result suggests that CeOMS-2 can replace advantageously a conventional carbon supported  $\text{MnO}_2$  catalyst in Zn/Air batteries and that BiOMS-2 can be used without a significant performance loss. It is a step forward in the obtention of non-noble metal oxide based bifunctional catalysts for metal-air batteries and alkaline fuel cells. To better understand the battery performance for each cathode catalyst studied, the electrochemical impedance response of the system at  $0.5 \text{ V}$  was used as probe, as presented in Fig. 9 by the corresponding Nyquist plots ( $Z'$  vs  $Z''$ ).

The impedance spectra of BiOMS-2 and CeOMS-2 consist of two semicircles, a small one in the high frequency range, left side, followed by a bigger one in the low frequency range, right side, as observed in Fig. 9B. The first semicircle in the high frequency range cannot be

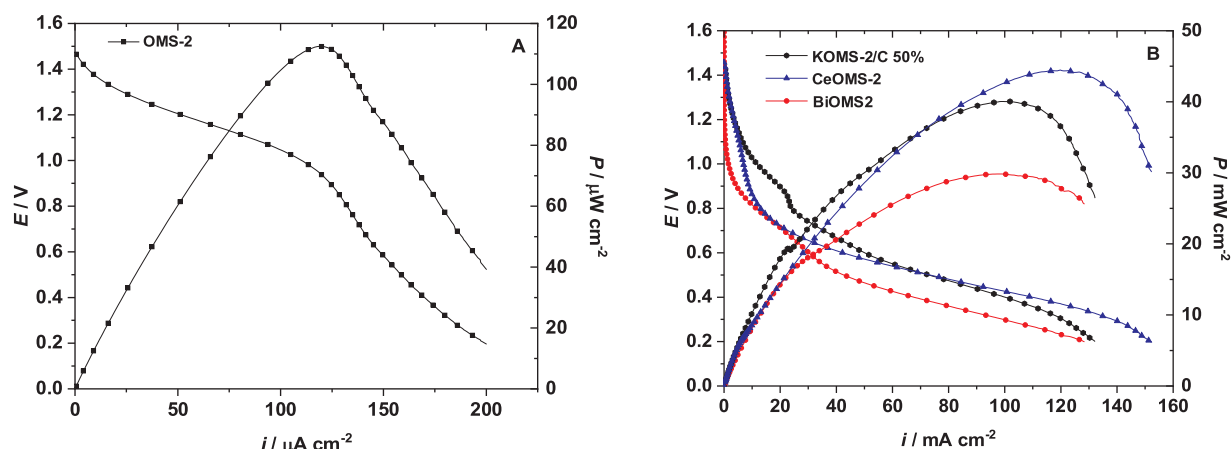


**Fig. 8.** Discharge curves and power density curves of (A) KOMS-2 ( $2.07 \text{ mg}_{\text{KOMS-2}} \text{ cm}^{-2}$ ) and (B) KOMS-2/C 50 wt.% ( $1.04 \text{ mg}_{\text{KOMS-2/C}} \text{ cm}^{-2}$ ), BiOMS-2 ( $2.07 \text{ mg}_{\text{BiOMS-2}} \text{ cm}^{-2}$ ) and CeOMS-2 ( $2.07 \text{ mg}_{\text{CeOMS-2}} \text{ cm}^{-2}$ ) based alkaline Zn/Air batteries.

clearly observed in the impedance spectra of KOMS-2 depicted in Fig. 9A probably masked by the huge system resistance associated with the KOMS-2 catalyst. To extract the impedance parameters, the spectra were fitted using equivalent circuits. The results are presented in Fig. 9B for the BiOMS-2 and CeOMS-2 catalysts and in Fig. S7 for KOMS-2. The equivalent circuit used is also illustrated in Fig. 8B, where R1 represents the electrolyte resistance, R2 the solid-electrolyte interface resistance, R3 the charge transfer resistance, QPE1-Q is a constant phase element associated with the solid-electrolyte interface charge and QPE2-Q is the constant phase element associated with the double layer charge. This model has been already used successfully to analyze impedance results of metal/air batteries, including Zn/air [40–42]. The impedance parameters obtained by fitting are presented in Table 2.

The results presented in Fig. 9 and summarized by the parameters in Table 2 showed good agreement with the electrochemical results presented previously. The resistance associated with the electrolyte conductivity, R1, is constant for all systems. In all cases the supporting electrolyte used was the same, KOH aqueous solution ( $6.0 \text{ mol L}^{-1}$ ). The interface resistance, R2 and the charge transfer resistance, R3, are all mainly related with the cathode catalyst (doped OMS-2 materials), since it was the only component that was changed in all cases. Apparently, the different dopants influence very strongly the resistivity of the catalysts studied as already suggested by the smaller band-gap values obtained from the DRS experiments. In fact, CeOMS-2 showed the lowest band-gap value, followed by Bi-OMS-2 and KOMS-2. The interface resistance and charge transfer resistance follow the same tendency.

**Table 2**

Impedance parameters obtained from Nyquist plots of KOMS-2, BiOMS-2 and CeOMS-2.

Parameter	Catalyst		
	BiOMS-2	CeOMS-2	KOMS-2
R1 [ $\Omega$ ]	1,48	1,43	1,45
R2 [ $\Omega$ ]	0,22	0,12	755
R3 [ $\Omega$ ]	2,68	2,58	799
QPE1-Q [F]	0.0025	0.0022	$2.83 \cdot 10^{-6}$
QPE1-n	0.58	0.57	0.77
QPE2-Q [F]	0.0067	0.0095	$8.62 \cdot 10^{-7}$
QPE2-n	0.96	0.87	0.85

The impedance results corroborate that the lowest CeOMS-2 resistivity facilitate the electron transfer from the catalyst surface to the oxygen molecules resulting in a better catalyst performance, as indicated by the ORR and OER results along with the better battery performance. The low catalyst and battery performances presented by KOMS-2 is mainly associated with the very large resistivity presented by this material. Therefore, all three results, ORR, OER and electrochemical impedance spectroscopy showed that doped OMS-2 nanomaterials are suitable as bifunctional cathode catalysts for metal/air batteries.

In order to evaluate the effect of catalyst loading on the Zn/air performance, an experiment using the double of the catalyst loading ( $6.16 \text{ mg cm}^{-2}$ ) of that presented in Fig. 8 was performed. The result is

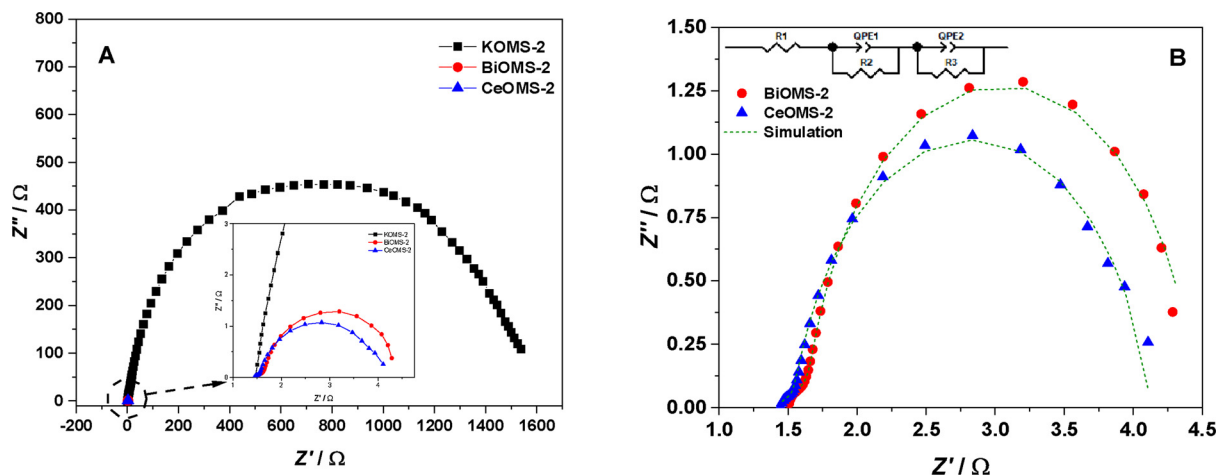


**Fig. 9.** Nyquist plots of (A) KOMS-2, BiOMS-2 and CeOMS-2 in the frequency range of 100 kHz–10 mHz with an AC signal amplitude of 10 mV at a polarization voltage of 0.5 V and (B) experimental and simulated impedance data for BiOMS-2 and CeOMS-2 catalysts at a polarization voltage of 0.5 V.

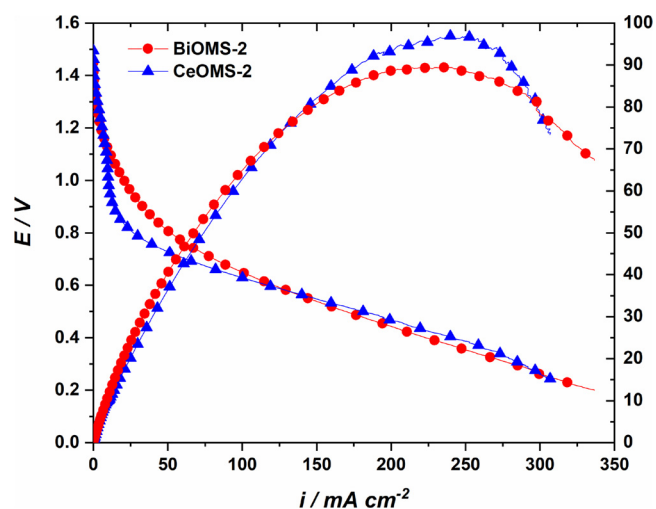


Fig. 10. Discharge and power density curves of BiOMS-2 ( $4.14 \text{ mg}_{\text{BiOMS-2}} \text{ cm}^{-2}$ ) and CeOMS-2 ( $4.14 \text{ mg}_{\text{CeOMS-2}} \text{ cm}^{-2}$ ) based alkaline Zn/Air batteries.

presented in Fig. 10. When the catalyst loading is increased, the battery performance is significantly increased, resulting in a power peak density of almost  $100 \text{ mW cm}^{-2}$  for the battery operating with CeOMS-2 as cathode catalyst. The increase of battery performance is certainly related in some extension with the increase of oxygen recycling resulted from the two-electron reduction pathway. The possibility of increasing the battery performance by increasing the catalyst loading is very interesting because the material used is non-expensive. Consequently, the development of batteries for applications that demands more energy can be adjusted by increasing the cathode catalyst loading.

### 3.2.5. Catalysts stability and performance tests after long term utilization

In order to evaluate the stability of the materials studied, as well as possible performance degradation of the catalyst's activity after long term utilization, chronopotentiometric experiments at low ( $7.0 \text{ mA cm}^{-2}$ ) and high ( $49.0 \text{ mA cm}^{-2}$ ) current densities were performed for 1 h in each case. The results are presented in Fig. 11 for CeOMS-2 and BiOMS-2 using low catalyst loadings ( $2.07 \text{ mg cm}^{-2}$ ). At such conditions, there is no signs of performance degradation, either for BiOMS-2 and CeOMS-2 at each current density value used. The potential values are practically constant all the time in each case and the potential values are compatible with that obtained for the Zn/Air

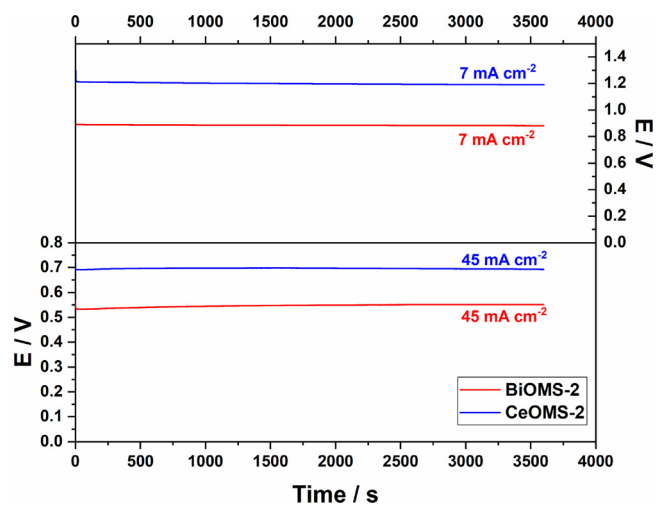


Fig. 11. Chronopotentiometric responses at  $7.0 \text{ mA cm}^{-2}$  and  $49 \text{ mA cm}^{-2}$  for the Zn/Air battery equipped with BiOMS-2 ( $2.07 \text{ mg}_{\text{BiOMS-2}} \text{ cm}^{-2}$ ) and CeOMS-2 ( $2.07 \text{ mg}_{\text{CeOMS-2}} \text{ cm}^{-2}$ ) as cathode catalysts.

battery discharge curve presented in Fig. 8 for BiOMS-2 and CeOMS-2 for the current densities considered.

In order to evaluate the catalysts after long term utilization to verify possible composition and structure changes, as well as possible Bi and Ce dopant losses, TEM images and EDS elemental mapping from STEM experiments were performed after the chronopotentiometric experiments. The results are presented in Figs. S8 and S9. Clearly, there is no signs of structure changes in each case, as observed by the TEM and HRTEM images provided for BiOMS-2 and CeOMS-2. As in the freshly prepared catalysts, the oxides are composed by nanorods without any other visible structure. The corroded CeOMS-2 has been already observed in the freshly prepared material and this is attributed to the acid treatment at which this material is submitted to allowing the doping with Ce. From the EDS elemental mapping, either Bi and Ce can be clearly observed for the corresponding cation doped catalysts. This result is consistent with that presented in Fig. 11, where no performance losses have been observed in the long-term electrochemical experiments using BiOMS-2 and CeOMS-2 as cathode catalysts. It is interesting to be observed that the Zn anode suffered from severe corrosion at the end of each experiment, indicating that the catalysts have been extensively used. Consequently, the cation doped  $\text{MnO}_2$  based catalysts have adequate stability to be used as cathode catalysts in alkaline Zn/Air batteries.

## 4. Conclusions

Bifunctional air cathodes based on carbon free manganese dioxide nanorod doped with potassium, bismuth and cerium cations have been successfully prepared and tested in a mini Zn/air alkaline battery. Based on SEM and TEM measurements, all catalyst materials have a rod like structure with 50–200 nm length and  $\sim 10 \text{ nm}$  width, typical of  $\alpha\text{-MnO}_2$  containing a central tunnel. The XRD measurements showed that the dopant cations were positioned inside the central tunnel which was also filled with water molecules. Using  $\text{Bi}^{3+}$  and  $\text{Ce}^{4+}$  cations as dopants, catalysts (BiOMS-2 and CeOMS-2) with lower band gap values than  $\text{K}^+$  doped  $\text{MnO}_2$  (KOMS-2), suggesting that materials with improved conductivity are produced. This property was confirmed by electrochemical measurements using the classical rotating disk electrode (RDE) configuration and a mini Zn/air battery with the cation doped  $\text{MnO}_2$  materials as air cathodes. The RDE measurements showed that BiOMS-2 and CeOMS-2 were capable to operate as carbon free cathode catalysts due to improved conductivity, whereas KOMS-2 showed significant resistance. Furthermore, BiOMS-2 and CeOMS-2 showed remarkable electrocatalytic activity, overcoming the activity of a commercial Pt/C 20 wt% catalyst in the kinetically controlled potential region which is the most significant for practical applications. Based on the mini Zn/air battery tests, the improved conductivity of BiOMS-2 and CeOMS-2 were also confirmed by electrochemical impedance spectroscopy measurements. Both catalysts presented much lower charge transfer resistance than KOMS-2 catalyst. The better battery performance was obtained using CeOMS-2 as the air cathode catalyst, in which case a peak power density of  $45 \text{ mW cm}^{-2}$  was obtained, higher than the value of  $40 \text{ mW cm}^{-2}$  obtained by using a conventional KOMS-2/C 50 wt.% cathode catalyst. The remarkable activity of BiOMS-2 and CeOMS-2 for the oxygen reduction reaction allied with the reasonable activity presented by these materials for the oxygen evolution reaction with a  $\Delta E_{\text{ORR/OER}} = 1.07 \text{ V}$  for BiOMS-2 and  $1.02 \text{ V}$  for CeOMS-2 indicate that these are very promising candidates to operate as bifunctional air cathode catalysts of metal/air batteries and alkaline fuel cells. The materials have been submitted to long term utilization experiments and no signs of performance and materials degradations have been observed, indicating that BiOMS-2 and CeOMS-2 are adequate and stable materials to be used as cathode catalysts in alkaline metal/air batteries.



## Author contributions

The manuscript was written through contributions of all authors, and all authors have given approval to the final version of the manuscript.

## Declaration of Competing Interest

The authors declare no competing financial interest.

## Acknowledgments

This work was supported by Brazilian agencies Fundação de Amparo à Pesquisa do Estado de São Paulo – FAPESP (Grant Nos. 2011/02158-5) and Conselho Nacional de Desenvolvimento Científico e Tecnológico – CNPq.

## Appendix A. Supplementary data

Supplementary material related to this article can be found, in the online version, at doi:<https://doi.org/10.1016/j.apcatb.2019.118014>.

## References

- [1] M. Arafat Rahman, X. Wang, C. Wen, High Energy Density Metal-Air Batteries: A Review, (2013).
- [2] V. Caramia, B. Bozzini, Materials science aspects of zinc-air batteries: a review, *Mater. Renew. Sustain. Energy* 3 (2014) 28.
- [3] Z.-L. Wang, D. Xu, J.-J. Xu, X.-B. Zhang, Oxygen electrocatalysts in metal-air batteries: from aqueous to nonaqueous electrolytes, *Chem. Soc. Rev.* 43 (2014) 7746–7786.
- [4] X. Zhang, X.-G. Wang, Z. Xie, Z. Zhou, Recent progress in rechargeable alkali metal-air batteries, *Green Energy Environ.* 1 (2016) 4–17.
- [5] P. Gu, M. Zheng, Q. Zhao, X. Xiao, H. Xue, H. Pang, Rechargeable zinc-air batteries: a promising way to green energy, *J. Mater. Chem. A* 5 (2017) 7651–7666.
- [6] Y. Li, J. Lu, Metal-air batteries: will they be the future electrochemical energy storage device of choice? *ACS Energy Lett.* 2 (2017) 1370–1377.
- [7] J. Fu, Z.P. Cano, M.G. Park, A. Yu, M. Fowler, Z. Chen, Electrically rechargeable zinc-air batteries: progress, challenges, and perspectives, *Adv. Mater.* 29 (2017) 1604685-n/a.
- [8] I. Roche, E. Chainet, M. Chatenet, J. Vondrak, Carbon-supported manganese oxide nanoparticles as electrocatalysts for the oxygen reduction reaction (ORR) in alkaline medium: physical characterizations and ORR mechanism, *J. Phys. Chem. C* 111 (2007) 1434–1443.
- [9] Y. Zhang, J. Zang, J. Huang, S. Zhou, H. Gao, Y. Wang, Microwave synthesis and properties of MnO<sub>2</sub>/CNTs non-precious metal catalyst for oxygen reduction reaction in alkaline solution, *J. Appl. Electrochem.* 48 (2018) 157–164.
- [10] Z. Zeng, W. Zhang, Y. Liu, P. Lu, J. Wei, Uniformly electrodeposited  $\alpha$ -MnO<sub>2</sub> film on super-aligned electrospun carbon nanofibers for a bifunctional catalyst design in oxygen reduction reaction, *Electrochim. Acta* 256 (2017) 232–240.
- [11] A. Flegler, S. Müssig, J. Prieschl, K. Mandel, G. Sextl, Towards core-shell bifunctional catalyst particles for aqueous metal-air batteries: NiFe-layered double hydroxide nanoparticle coatings on  $\gamma$ -MnO<sub>2</sub> microparticles, *Electrochim. Acta* 231 (2017) 216–222.
- [12] H. Zheng, M. Modibedi, M. Mathe, K. Ozoemena, The thermal effect on the catalytic activity of MnO<sub>2</sub> ( $\alpha$ ,  $\beta$ , and  $\gamma$ ) for oxygen reduction reaction, *Mater. Today Proc.* (2017) 11624–11629.
- [13] C.W. Woon, M.A. Islam, B. Ethiraj, H.R. Ong, C.K. Cheng, K.F. Chong, G. Hedge, M.M.R. Khan, Carbon nanotube-modified MnO<sub>2</sub>: an efficient electrocatalyst for oxygen reduction reaction, *ChemistrySelect* 2 (2017) 7637–7644.
- [14] M.C. Wu, T.S. Zhao, H.R. Jiang, L. Wei, Z.H. Zhang, Facile preparation of high-performance MnO<sub>2</sub>/KB air cathode for Zn-air batteries, *Electrochim. Acta* 222 (2016) 1438–1444.
- [15] Y. Li, H. Dai, Recent advances in zinc-air batteries, *Chem. Soc. Rev.* 43 (2014) 5257–5275.
- [16] X. Zhang, P. Yu, D.L. Wang, Y.W. Ma, Controllable synthesis of  $\alpha$ -MnO<sub>2</sub> nanostructures and phase transformation to  $\beta$ -MnO<sub>2</sub> microcrystals by hydrothermal crystallization, *J. Nanosci. Nanotechnol.* 10 (2010) 898–904.
- [17] R.N. Deguzman, Y.F. Shen, E.J. Neth, S.L. Suib, C.L. Oyoung, S. Levine, J.M. Newsam, Synthesis and characterization of octahedral molecular-sieves (OMS-2) having the hollandite structure, *Chem. Mater.* 6 (1994) 815–821.
- [18] H. Rietveld, A profile refinement method for nuclear and magnetic structures, *J. Appl. Crystallogr.* 2 (1969) 65–71.
- [19] R.B. Valim, M.C. Santos, M.R.V. Lanza, S.A.S. Machado, F.H.B. Lima, M.L. Calegario, Oxygen reduction reaction catalyzed by epsilon-MnO<sub>2</sub>: influence of the crystalline structure on the reaction mechanism, *Electrochim. Acta* 85 (2012) 423–431.
- [20] V.A. Paganin, E.A. Ticianelli, E.R. Gonzalez, Development and electrochemical studies of gas diffusion electrodes for polymer electrolyte fuel cells, *J. Appl. Electrochem.* 26 (1996) 297–304.
- [21] A.S. Bondarenko, G.A. Ragoisha, Progress in Chemometrics Research, Nova Science Publishers, New York, 2005.
- [22] N. Kijima, T. Ikeda, K. Oikawa, F. Izumi, Y. Yoshimura, Crystal structure of an open-tunnel oxide  $\alpha$ -MnO<sub>2</sub> analyzed by rietveld refinements and MEM-based pattern fitting, *J. Solid State Chem.* 177 (2004) 1258–1267.
- [23] Y. Yuan, C. Zhan, K. He, H. Chen, W. Yao, S. Sharifi-Asl, B. Song, Z. Yang, A. Nie, X. Luo, H. Wang, S.M. Wood, K. Amine, M.S. Islam, J. Lu, R. Shahbazian-Yassar, The influence of large cations on the electrochemical properties of tunnel-structured metal oxides, *Nat. Commun.* 7 (2016) 13374.
- [24] K. King'andu Cecil, N. Opembe, C.H. Chen, K. Ngala, H. Huang, A. Iyer, F. Garcés Hector, L. Suib Steven, Manganese oxide octahedral molecular sieves (OMS-2) multiple framework substitutions: a new route to OMS-2 particle size and morphology control, *Adv. Funct. Mater.* 21 (2010) 312–323.
- [25] X. Peng, Y. Guo, Q. Yin, J. Wu, J. Zhao, C. Wang, S. Tao, W. Chu, C. Wu, Y. Xie, Double-exchange effect in two-dimensional MnO<sub>2</sub> nanomaterials, *J. Am. Chem. Soc.* 139 (2017) 5242–5248.
- [26] T. Gao, M. Glerup, F. Krumeich, R. Nesper, H. Fjellvåg, P. Norby, Microstructures and spectroscopic properties of cryptomelane-type manganese dioxide nanofibers, *J. Phys. Chem. C* 112 (2008) 13134–13140.
- [27] F.H.B. Lima, M.L. Calegario, E.A. Ticianelli, Electrocatalytic activity of manganese oxides prepared by thermal decomposition for oxygen reduction, *Electrochim. Acta* 52 (2007) 3732–3738.
- [28] J. McBreen, Electrochemistry of beta-MnO<sub>2</sub> and gamma-MnO<sub>2</sub> in alkaline electrolyte, *Electrochim. Acta* 20 (1975) 221–225.
- [29] F.H.B. Lima, M.L. Calegario, E.A. Ticianelli, Investigations of the catalytic properties of manganese oxides for the oxygen reduction reaction in alkaline media, *J. Electroanal. Chem.* 590 (2006) 152–160.
- [30] M.L. Calegario, F.H.B. Lima, E.A. Ticianelli, Oxygen reduction reaction on nanosized manganese oxide particles dispersed on carbon in alkaline solutions, *J. Power Sources* 158 (2006) 735–739.
- [31] A.J. Bard, L.R. Faulkner, *Electrochemical Methods: Fundamentals and Applications*, 2nd ed., John Wiley & Sons, Inc., Toronto, Canada, 2000.
- [32] CRC Handbook of Chemistry and Physics, 57 ed., CRC Press, Inc., 1977.
- [33] R.E. Davis, G.L. Horvath, C.W. Tobias, Solubility and diffusion coefficient of oxygen in potassium hydroxide solutions, *Electrochim. Acta* 12 (1967) 287–8.
- [34] E.R. Vago, E.J. Calvo, Electroreduction of oxygen on Fe<sub>3</sub>O<sub>4</sub> electrodes. 2. Rotating ring-disc electrode studies and mechanism, *J. Chem. Soc. Faraday Trans.* 91 (1995) 2323–2329.
- [35] Y. Matsumoto, E. Sato, Electrocatalytic properties of transition-metal oxides for oxygen evolution reaction, *Mater. Chem. Phys.* 14 (1986) 397–426.
- [36] Y.X. Zhao, C. Chang, F. Teng, Y.F. Zhao, G.B. Chen, R. Shi, G.I.N. Waterhouse, W.F. Huang, T.R. Zhang, Defect-engineered ultrathin delta-MnO<sub>2</sub> nanosheet arrays as bifunctional electrodes for efficient overall water splitting, *Adv. Energy Mater.* 7 (2017).
- [37] G.Q. Han, X. Li, X. Zhao, B. Dong, W.H. Hu, Y.R. Liu, X. Shang, Y.M. Chai, C.G. Liu, Self-sacrificial template method to MnO<sub>2</sub> microspheres as highly efficient electrocatalyst for oxygen evolution reaction, *J. Solid State Electr.* 20 (2016) 2907–2912.
- [38] Y.T. Meng, W.Q. Song, H. Huang, Z. Ren, S.Y. Chen, S.L. Suib, Structure-property relationship of bifunctional MnO<sub>2</sub> nanostructures: highly efficient, ultra-stable electrochemical water oxidation and oxygen reduction reaction catalysts identified in alkaline media, *J. Am. Chem. Soc.* 136 (2014) 11452–11464.
- [39] Y. Gorlin, T.F. Jaramillo, A bifunctional nonprecious metal catalyst for oxygen reduction and water oxidation, *J. Am. Chem. Soc.* 132 (2010) 13612–13614.
- [40] Z. Chen, A. Yu, D. Higgins, H. Li, H. Wang, Z. Chen, Highly active and durable core-corona structured bifunctional catalyst for rechargeable metal-air battery application, *Nano Lett.* 12 (2012) 1946–1952.
- [41] Y. Kim Jae, J.W. Jang, H. Youn Duck, G. Magesh, S. Lee Jae, Photochemistry: a stable and efficient hematite photoanode in a neutral electrolyte for solar water splitting: towards stability engineering (Adv. Energy Mater. 13/2014), *Adv. Energy Mater.* 4 (2014).
- [42] M. Prabu, P. Ramakrishnan, H. Nara, T. Momma, T. Osaka, S. Shanmugam, Zinc-air battery: understanding the structure and morphology changes of graphene-supported CoMn<sub>2</sub>O<sub>4</sub> bifunctional catalysts under practical rechargeable conditions, *ACS Appl. Mater. Interface* 6 (2014) 16545–16555.